Chinese Chemical Letters 37 (2026) 111003

Contents lists available at ScienceDirect

Chinese Chemical Letters

journal homepage: www.elsevier.com/locate/cclet

Molecular tweezers in thiolate-protected Cu(I) clusters: A framework platform for investigating ligand effects in cluster catalysis

Jiaojiao Zhang[a,1], Yifan Wu[a,b,1], Yifei Li[a], Fuxing Lin[b,*], Shengchang Xiang[a], Xi Fan[a,*], Zhangjing Zhang[a,*]

[a] College of Chemistry and Materials Science, Fujian Normal University, Fuzhou 350117, China
[b] College of Resources and Chemical Engineering, Sanming University, Sanming 365004, China

ARTICLE INFO

Article history:
Received 21 December 2024
Revised 16 February 2025
Accepted 25 February 2025
Available online 25 February 2025

Keywords:
Coinage metal clusters
Cu nanoclusters
Framework
Molecular tweezers
Ligand effects

ABSTRACT

Scarce investigations have focused on coinage metal clusters possessing fixed cores but varying binding ligands in the context of catalysis. Here in this work, we successfully employed two types of carboxylic acid-based molecular tweezers to selectively capture two Cu_6 clusters (**Cu_6-a** and **Cu_6-b**). **Cu_6-a** and **Cu_6-b** have identical cluster cores but different protected ligands, therefore provide accurate platform for investigating ligand effects in cluster catalysis. Notably, **Cu_6-b** represents a rare example of a two-directional rod framework, marking the first instance of such a structure in coinage metal cluster-based MOFs. The integration of oxygen within OBB significantly enhances local spatial polarization, facilitating the charge separation and ROS generation efficiency of **Cu_6-b** under visible-light irradiation. Consequently, the oxygen-containing **Cu_6-b** exhibits superior photocatalytic performance in the aerobic oxidation of sulfide, achieving both high yield and selectivity. This work provides a valuable approach for precisely control the Cu clusters structures to regulate their properties.

© 2026 Published by Elsevier B.V. on behalf of Chinese Chemical Society and Institute of Materia Medica, Chinese Academy of Medical Sciences.

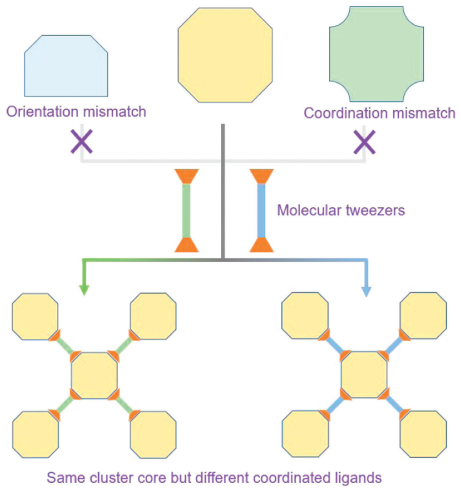
Homogeneities and atomically precise coinage metal clusters (Cu, Ag, and Au) serve as precise platforms for bridging the gap between small metal-ligand molecules and metal nano-solids [1–5]. Consequently, they are selected as model catalysts due to their well-defined compositions and adjustable structures, establishing a robust foundation for correlating structures with properties [6–10]. Various ligands have been utilized to fabricate a range of coinage metal nanoclusters. It has been observed that surface ligands not only shield the metal core but also influence the catalytic properties, particularly the activity [11–15]. To comprehend the ligand effect involved in nanocluster catalysis, metal nanoclusters with fixed nuclearities but varying binding ligands serve as ideal model catalysts.

Owing to the weak metal-metal interactions and the diverse ligand-metal coordination, the structure of metal clusters exhibits considerable variability [16–18]. Generally, following the completion of a reaction, isolated single-crystalline metal clusters are not the exclusive synthesized product. They may be just more prevalent in yield or more readily form in saturated solutions, thereby facilitating crystallization. However, these conditions are notably sensitive, and even minor adjustments in the synthesis of metal clusters can lead to substantial alterations in the isolated cluster nuclei [19–23]. Moreover, guest solvents within the clusters tend to exhibit high volatility, resulting in the loss of crystallinity and presenting significant stability issues [24]. Consequently, only a limited number of investigations have focused on coinage metals possessing fixed cores but varying binding ligands in the context of catalysis [25–27].

Metal–organic frameworks constructed from novel cluster building blocks are fundamental aspects of reticular chemistry, representing naturally self-assembled superlattices of metal nanoparticles [28]. Both MOFs and coinage metal clusters have garnered extensive research attention. However, MOFs based on coinage metal clusters have received relatively scant attention, with only a handful of coinage metal clusters capable of serving as construction units for cluster-based frameworks [29]. Attaching clusters to adaptable bridging ligands enables their interconnection and the formation of robust cluster-based frameworks. These spatially separated clusters are likely to exhibit enhanced stability and unique properties compared to their monomeric counterparts. One crucial aspect of forming such supramolecular architectures is the use of effective building blocks, which provide ligand-accessible coordination sites with desired spatial orientations for assembly into ar-

* Corresponding authors.
E-mail addresses: fuxingangel@163.com (F. Lin), fanxi@fjnu.edu.cn (X. Fan), zzhang@fjnu.edu.cn (Z. Zhang).
[1] These authors contributed equally to this work.

https://doi.org/10.1016/j.cclet.2025.111003
1001-8417/© 2026 Published by Elsevier B.V. on behalf of Chinese Chemical Society and Institute of Materia Medica, Chinese Academy of Medical Sciences.



Scheme 1. Illustration of molecular tweezers selecting metal clusters with identical cores.

chitectures. In other words, the role of bridging ligands can also be viewed as acting like molecular tweezers, selectively picking preferred clusters and expediting their crystallization process. This eliminates the influence of factors such as inter-cluster interactions and solubility in solution on the resulting crystallized clusters. By employing tweezers with similar coordination preferences, it is possible to extract identical metal cluster building units, thereby enhancing stability and providing a platform to investigate the impact of ligands on cluster core catalytic performance (Scheme 1).

In this study, we successfully employed two types of carboxylic acid-based molecular tweezers to selectively capture two Cu_6 clusters (**Cu_6-a** and **Cu_6-b**). They have identical cluster cores but different protected ligands, therefore provide accurate platform for investigating ligand effects in cluster catalysis. The incorporation of oxygen in OBB significantly enhances local spatial polarization, facilitating the charge separation and ROS generation efficiency of **Cu_6-b** under visible-light irradiation. As a results, the oxygen-containing **Cu_6-b** exhibits superior photocatalytic performance in the aerobic oxidation of sulfide, achieving both high yield and selectivity.

Solvothermal reaction of $Cu(TFA)_2{\cdot}xH_2O$, 2-methyl-2-propanethiol (MPT) with 4,4′-biphenyl dicarboxylic acid (BPDC) in the present of Ph_2SiH_2 at 90 °C produced yellow needle-like crystals of **Cu_6-a**. Single-crystal X-ray diffraction (SCXRD) analysis reveals that **Cu_6-a** crystallizes in the monoclinic space group $I_{2/a}$ (Table S1 in Supporting information). The building units of **Cu_6-a** resemble trigonal prismatic Cu_6 clusters, stabilized by 4 MPT and 2 carboxylic acid ligands (Fig. 1a), indicating that Cu in **Cu_6-a** exists as Cu(I), and **Cu_6-a** contains no free valence electron (6 – 4 – 2 = 0) (Fig. 1a). The Cu···Cu distances range from 2.725 Å to 3.067 Å (Fig. S1 in Supporting information), highlight the notable cuprophilic interactions within **Cu_6-a**. 4 MPT ligands adopt two types of coordination modes with Cu atoms (μ_4-η^1, η^1, η^1, $\eta^1 \times 2$; μ_3-η^1, η^1, $\eta^1 \times 2$), and the Cu-S bond lengths range from 2.191 Å to 2.352 Å (Fig. S2 in Supporting information). The Cu_6 units are linked into 1D rods *via* MPT ligands and then arranged into a framework structure, assisted by BPDC ligands (Figs. 1b-d). Interpenetrating of two such frameworks result in the formation of the final **Cu_6-a** structure (Figs. 1e and f), leading to a reduced cavity size and potentially enhancing its structural stability. All the rods in **Cu_6-a** point in one direction.

The less-than-optimal yield of **Cu_6-a** indicates that Cu_6 is clearly not the exclusive metal cluster product in this solvent reaction. BPDC can be likened to molecular tweezers, effectively selecting preferred Cu_6 clusters and enhancing their crystallization rate. Therefore, employing another tweezer with similar coordination tendencies may aid in isolating identical Cu_6 clusters. Analogously, substituting linear 4,4′-biphenyldicarboxylic acid ligands with V-shaped 4,4′-oxybisbenzoic acid ligands (OBB) yields different crystals of **Cu_6-b**. As expected, **Cu_6-b** possess identical Cu_6 building unit with **Cu_6-b**, which are also linked into same 1D rods *via* MPT ligands (Figs. 1c and g). However, due to the V-shaped OBB ligands, the rods propagate along the a- and b-axes in **Cu_6-b** (Figs. 1h and i). It is noteworthy that one-directional straight rod SBUs, like those in **Cu_6-a**, dominate the rod frameworks. While two-directional rod frameworks, where rods propagate along both the a- and b-axes, are rare [30]. Therefore, **Cu_6-b** represents a significant addition to the scarce family of two-directional rod frameworks, which represents the first instance in coinage metal clusters-based MOFs.

This pair of isostructural Cu_6 based rods frameworks provides us with a valuable opportunity to accurately study the ligand-oriented catalytic properties in Cu clusters. To evaluate the optical properties of **Cu_6-a** and **Cu_6-b**, UV–vis diffuse reflectance spectroscopy (DRS) measurements were performed. As shown in Fig. 2a, both materials exhibit absorption edges extending beyond 500 nm, indicating their partial capacity to absorb visible light. The slightly red-shift observed in **Cu_6-b** compared to **Cu_6-a**, suggesting that **Cu_6-b** exhibits a stronger response to visible light. Furthermore, the optical bandgaps of **Cu_6-a** and **Cu_6-b** were investigated based on the Tauc plots. The E_g values for **Cu_6-a** and **Cu_6-b** were determined to be 2.55 eV and 2.50 eV, respectively (Fig. S7 in Supporting information). To ascertain the conduction band (CB) positions, Mott-Schottky (MS) electrochemical measurements were conducted (Fig. S8 in Supporting information). The E_{CB} values were estimated to be −0.58 V and −0.62 V *versus* Ag/AgCl (−0.48 V and −0.52 V *versus* NHE). Consequently, the valence band (VB) positions were thus calculated to be 2.07 V (**Cu_6-a**), and 1.98 V (**Cu_6-b**) *versus* NHE by using the equation ($E_g = E_{VB} - E_{CB}$) (Fig. 2b). Photocurrent measurements corroborated enhanced charge separation efficiency in **Cu_6-b** over **Cu_6-a**, evidenced by significantly higher photocurrent intensity recorded for **Cu_6-b** (Fig. 2c). Electrochemical impedance spectroscopy (EIS) plots demonstrated a gradual decrease in interfacial charge transfer resistance from **Cu_6-a** to **Cu_6-b** (Fig. 2d).

The CB positions of **Cu_6-a** and **Cu_6-b** possess more negative potentials than that of the $O_2/O_2^{\bullet-}$ redox couple (−0.33 V *versus* NHE), indicating that the generation of reactive oxygen species (ROS) is thermodynamically favorable. In the presence of photocatalysts and molecular oxygen, two types of ROS, superoxide radical ($O_2^{\bullet-}$) and singlet oxygen ($^1O_2$), are typically produced. Consequently, electron paramagnetic resonance (EPR) measurements were conducted to confirm the formation of both $O_2^{\bullet-}$ and $^1O_2$. The presence of $^1O_2$ was verified using 2,2,6,6-tetramethylpeperidine (TEMP) as trapping agent, while 5,5-dimethylpyrroline-*N*-oxide (DMPO) was employed for the detection of $O_2^{\bullet-}$. The distinctive triplet signals of $^1O_2$, characterized by the ratio of 1:1:1, are prominently observable in the EPR spectrum, with **Cu_6-b** exhibiting a more pronounced signal for $^1O_2$ in comparison to **Cu_6-a** (Fig. 2e). Additionally, **Cu_6-a** displayed weak six-line EPR signals indicative of $O_2^{\bullet-}$ formation; however, signal intensity observed with **Cu_6-b** exceeded that seen with **Cu_6-a** (Fig. 2f). The higher peak intensities suggest a greater efficiency in free radical generation. Consequently, **Cu_6-b** demonstrates superior yields of both singlet oxygen and superoxide radicals compared to **Cu_6-a**.

Given the differential capacities of **Cu_6-a** and **Cu_6-b** in generating reactive oxygen species, we further compared their photocatalytic potential in the oxidation of thioethers under visible light irradiation at room temperature. Specifically, **Cu_6-b** demonstrated superior photocatalytic performance in the oxidation of thioalkyl

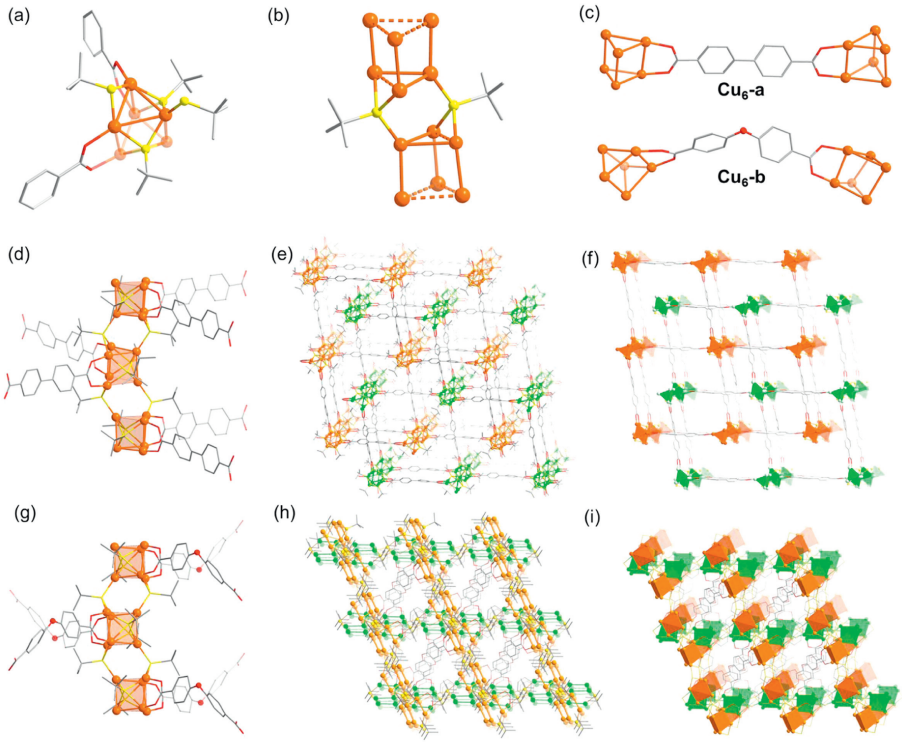


Fig. 1. (a) The structure of the building block of Cu_6 cluster. (b) Bridge linker MPT between the adjacent Cu_6 clusters. (c) Carboxylic acid-based molecular tweezers capture two Cu_6 clusters. (d) The chain, (e) the double-interpenetrated 3D framework and (f) its polyhedral model of **Cu_6-a**. (g) The chain, (h) the crosswise 3D framework and (i) its polyhedral model of **Cu_6-b**. Atom color codes: Cu, orange or green; O, red; C, gray; S, yellow. H atoms are omitted for clarity.

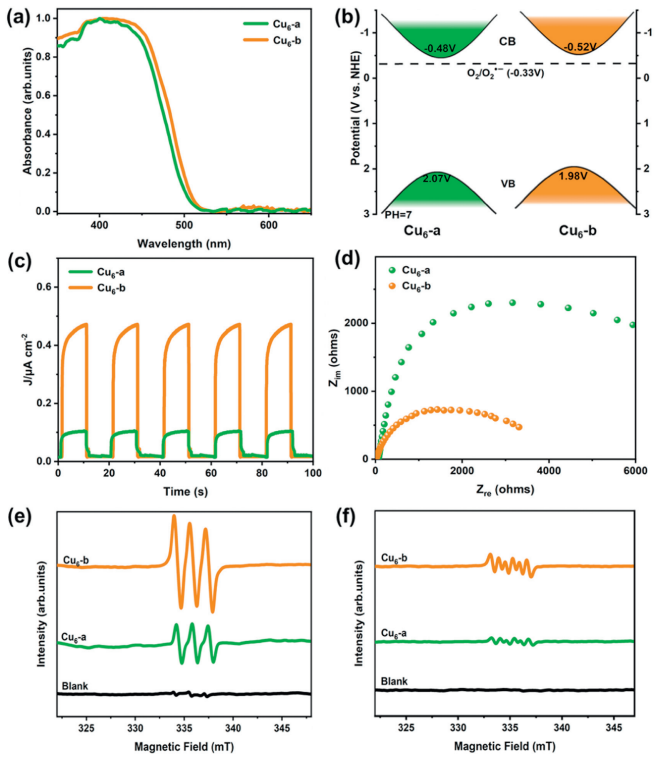
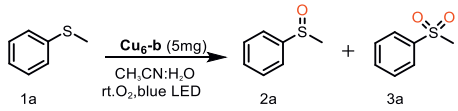


Fig. 2. (a) The UV-visible diffuse reflectance spectrum (UV–vis DRS) of **Cu_6-a** and **Cu_6-b**. (b) Schematic illustration for the band structures of **Cu_6-a** and **Cu_6-b**. (c) Photocurrent of **Cu_6-a** and **Cu_6-b** under visible light irradiation. (d) The EIS plots of **Cu_6-a** and **Cu_6-b**. EPR spectra of **Cu_6-a** and **Cu_6-b** in the presence of (e) TEMP-$^1O_2$ and (f) DMPO-$O_2^{\bullet-}$ under visible light irradiation.

Table 1
Visible-light-driven aerobic oxidation of thioanisole.[a]

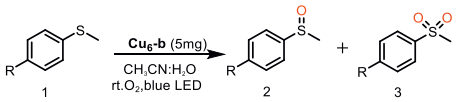


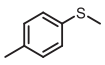
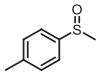
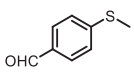
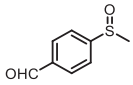
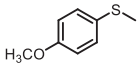
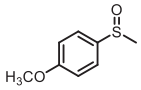
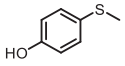
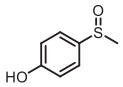
Entry	Change from the "standard conditions"	Conv. (%)[b]	Sel. (**2a**:**3a**, %)[b]
1	None	99	95
2	No light	Trace	–
3	Under N_2, instead of air	Trace	–
4	No **Cu_6-b**	Trace	–
5	Green LED, instead of blue LED	Trace	–
6	Red LED, instead of blue LED	Trace	–
7	3.0 mg **Cu_6-b**	90	95
8	**Cu_6-a** instead of **Cu_6-b**	8	>99

[a] Reaction conditions: **1a** (0.20 mmol), **Cu_6-b** (5.0 mg), acetonitrile (2.0 mL), H_2O (1 mL), r.t., 4 h, **Cu_6-a** (5.0 mg), r.t., 12 h blue light-emitting diode (LED), in an O_2 atmosphere.
[b] Determined by ^1H NMR analysis of the crude reaction mixture.

methyl ether under blue light, achieving conversions exceeding 99 % within 4 h (Table 1, Figs. S9 and S11 in Supporting information). In contrast, when **Cu_6-a** was used as the photocatalyst under similar conditions, the conversion dropped to merely 8 % even after 12 h, which correlates with its efficiency in generating reactive oxygen species (Table 1, Figs. S10 and S11 in Supporting information). The catalytic performance of **Cu_6-b** remains consistent across three cycles and no significant structural alterations were observed as confirmed by PXRD and FTIR spectra (Figs. S12-S14 in Supporting information). Control experiments conducted in darkness, under a nitrogen atmosphere, or without **Cu_6-b** showed negligible conversion rates, indicating that light, oxygen, and **Cu_6-b** are all essential for this reaction (Table 1, entries 2–4). Furthermore, the photocat-

Table 2
Visible-light-driven aerobic oxidation of sulfide derivatives.[a]



Entry	Substrate	Product	Yield (%)[b]	Sel. (**2**:**3**, %)[b]
1			99	95
2			95	93
3			98	93
4			99	98
5			99	94

[a] Reaction conditions: **1a** (0.20 mmol), **Cu_6-b** (5.0 mg), acetonitrile (2.0 mL), H_2O (1 mL), r.t., 4 h, blue light-emitting diode (LED), in an O_2 atmosphere.
[b] Determined by ^1H NMR analysis of the crude reaction mixture.

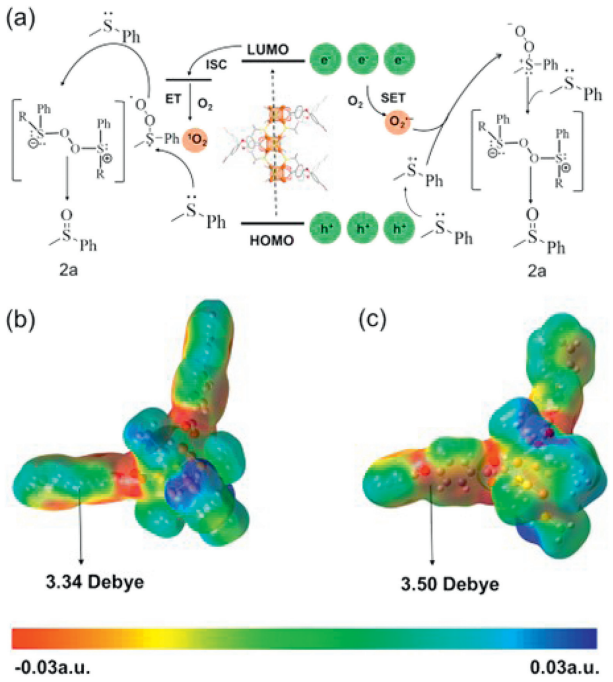


Fig. 3. (a) Possible reaction mechanism of the photocatalytic thioether oxidation of **Cu_6-b**. The molecular dipole of (b) **Cu_6-a** and (c) **Cu_6-b.**

alytic efficacy of **Cu_6-b** significantly decreased as the wavelength of the light source increased, suggesting that blue light energy is crucial for electronic excitation in this context (Table 1, entries 5 and 6).

After optimizing the reaction conditions, we further investigated the substrate scope that could be applied in this reaction using **Cu_6-b** as the catalyst (Table 2). The sulfones produced through the photocatalytic oxidation of substituted thioanisole derivatives exhibited remarkable yields and selectivity. A wide range of phenyl sulfide substrates, whether containing electron-withdrawing groups (-CHO) or electron-donating groups (-CH_3, –OCH_3, or -OH), were successfully converted into their corresponding sulfoxides. Importantly, there was no cooxidation observed with adjacent hydroxyl or carbonyl functionalities. This finding suggests a high degree of functional group tolerance during this gentle oxidation process (Figs. S9 and S15-S18 in Supporting information).

In order to further investigate the photocatalytic oxidation of thioether, we conducted radical quenching experiments. The yield of sulfoxide significantly dropped when L-histidine (L-His) and *p*-benzoquinone (BQ) was employed as $^1O_2$ and $O_2^{\bullet-}$ quenchers, respectively, with L-His causing a greater reduction (Figs. S19 and S20 in Supporting information). These results clearly indicate that both $O_2^{\bullet-}$ and $^1O_2$ play significant roles in the synthesis of sulfoxides, and that $^1O_2$ is the predominant species in the photocatalytic oxidation of thioethers. Additionally, the introduction of *t*-BuOH as a hydroxyl radical (·OH) scavenger did not result in a significant decrease in the yield of compound **2a**. This observation excludes the participation of the ·OH pathway in the photocatalytic oxidation process of thioethers (Fig. S21 in Supporting information).

According to the data presented above, we propose analogous mechanisms for the photocatalytic oxidations. Initially, upon visible light irradiation, electrons in the HOMO of **Cu_6** are excited into the LUMO, generating free electrons and positively charged holes. Subsequently, O_2 is activated into $^1O_2$ and $O_2^{\bullet-}$ through energy transfer (ET) and singlet electron transfer (SET) processes, respectively. The ET process involves the formation of a phenyl sulfide radical cation *via* the interaction of $^1O_2$ with phenyl sulfide. This radical cation then reacts with another phenyl sulfide to produce the desired product, phenyl sulfoxide. Additionally, photo-generated hole oxidizes the phenyl sulfide to its corresponding radical cation. In the SET process, the interaction between the phenyl sulfide radical cation and $O_2^{\bullet-}$ results in the formation of an intermediate peroxysulfoxide, which further reacts with additional phenyl sulfide molecules to generate target phenyl sulfoxide. Consequently, the synergistic effects of both ET and CT processes facilitate the production of this end productphenyl sulfoxide (Fig. 3a).

Polarization can be utilized to modulate the optical and electrical properties of solid-state materials, enhancing their charge transfer efficiency [31]. To gain a deeper understanding of the distinct optical and electrochemical properties between **Cu_6-a** and **Cu_6-b**, we calculated the dipole moments of the two component fragments depicted in the figure using the density functional theory (DFT) method with the M06–2X/def2tzvp basis set. The dipole moments of the two component fragments in the figure were calculated through the density functional theory (DFT) of the M06–2X/def2tzvp method. The results revealed that **Cu_6-b** exhibits a dipole moment of 3.50 Debye, surpassing that of **Cu_6-a** at 3.34 Debye (Figs. 3b and c). Therefore, the incorporation of oxygen in OBB significantly enhances local spatial polarization and favors the creation of a robust internal electric field, thereby accelerating in-plane charge transfer and facilitating efficient in-plane charge separation.

In summary, we successfully employed two types of carboxylic acid-based molecular tweezers to selectively capture two Cu_6 clusters (**Cu_6-a** and **Cu_6-b**). A noteworthy aspect of **Cu_6-b** is its unique two-directional rod framework, which represents the first example within coinage metal cluster-based MOFs. Both **Cu_6-a** and **Cu_6-b** share identical cluster cores but different protected ligands, therefore provide accurate platform for investigating ligand effects in cluster catalysis. The incorporation of oxygen in OBB significantly enhances local spatial polarization, facilitating the charge separation and ROS generation efficiency of **Cu_6-b** under visible-light irradiation. As a result, the oxygen-containing **Cu_6-b** exhibits superior photocatalytic performance in the aerobic oxidation of sul-

fide, achieving both high yield and selectivity. This work provides a valuable approach for precisely control the Cu clusters structures to regulate their properties.

Declaration of competing interest

The authors declare that they have no known competing financial interests or personal relationships that could have appeared to influence the work reported in this paper.

CRediT authorship contribution statement

Jiaojiao Zhang: Writing – original draft, Methodology, Formal analysis, Data curation. **Yifan Wu:** Formal analysis. **Yifei Li:** Formal analysis. **Fuxing Lin:** Resources. **Shengchang Xiang:** Resources. **Xi Fan:** Writing – review & editing, Writing – original draft, Supervision, Conceptualization. **Zhangjing Zhang:** Writing – review & editing, Conceptualization.

Acknowledgments

This work was supported by National Natural Science Foundation of China (Nos. 22101048, 22271046 and 22373015), the National Science Fund for Distinguished Young Scholars of China (No. 22425102), the Natural Science Foundation of Fujian Province (No. 2021J01150).

Supplementary materials

Supplementary material associated with this article can be found, in the online version, at doi:10.1016/j.cclet.2025.111003.

References

[1] G. Deng, B.K. Teo, N. Zheng, J. Am. Chem. Soc. 143 (2021) 10214–10220.
[2] Y.L. Liu, S.Z. Zhan, J.X. Sun, et al., Angew. Chem. Int. Ed. 62 (2023) e202306748.
[3] W.D. Liu, J.Q. Wang, S.F. Yuan, et al., Angew. Chem. Int. Ed. 60 (2021) 11430–11435.
[4] Y.-P. Xie, Y.L. Shen, G.X. Duan, et al., Mater. Chem. Front. 4 (2020) 2205–2222.
[5] X. Kang, M. Zhu, Chem. Soc. Rev. 48 (2019) 2422–2457.
[6] S.F. Yuan, R.L. He, X.S. Han, et al., Angew. Chem. Int. Ed. 60 (2021) 14345–14349.
[7] X.K. Wan, J.Q. Wang, Q.M. Wang, Angew. Chem. Int. Ed. 60 (2021) 20748–20753.
[8] X. Du, R. Jin, ACS Nano 13 (2019) 7383–7387.
[9] L.J. Liu, Z.Y. Wang, Z.Y. Wang, et al., Angew. Chem. Int. Ed. 61 (2022) e202205626.
[10] X. Fan, J. Cheng, M. Qiu, et al., ACS Mater. Lett. 5 (2023) 1527–1531.
[11] L. Chen, F. Sun, Q. Shen, et al., Nano Res. 15 (2022) 8908–8913.
[12] Q. Tang, G. Hu, V. Fung, et al., Acc. Chem. Res. 51 (2018) 2793–2802.
[13] H. Liang, B.J. Liu, B. Tang, et al., ACS Catal. 12 (2022) 4216–4226.
[14] Z.Y. Wang, M.Q. Wang, Y.L. Li, et al., J. Am. Chem. Soc. 140 (2018) 1069–1076.
[15] J. Wang, F. Xu, Z.Y. Wang, et al., Angew. Chem. Int. Ed. 61 (2022) e202207492.
[16] Z. Lei, X.K. Wan, S.F. Yuan, et al., Acc. Chem. Res. 51 (2018) 2465–2474.
[17] H.Y. Zhuo, H.F. Su, Z.Z. Cao, et al., Chem. Eur. J. 22 (2016) 17619–17626.
[18] S. Li, Z.Y. Wang, G.G. Gao, et al., Angew. Chem. Int. Ed. 57 (2018) 12775–12779.
[19] X. Fan, F. Yuan, J. Wang, et al., CCS Chem. 5 (2023) 350–360.
[20] X. Fan, F. Yuan, D. Li, et al., Angew. Chem. Int. Ed. 60 (2021) 12949–12954.
[21] B.L. Han, Z. Liu, L. Feng, et al., J. Am. Chem. Soc. 142 (2020) 5834–5841.
[22] S. Hossain, Y. Imai, D. Suzuki, et al., Nanoscale 11 (2019) 22089–22098.
[23] X. Kang, M. Zhu, Chem. Soc. Rev. 48 (2019) 2422–2457.
[24] R.W. Huang, Y.S. Wei, X.Y. Dong, et al., Nat. Chem. 9 (2017) 689–697.
[25] Q.J. Wu, D.H. Si, P.P. Sun, et al., Angew. Chem. Int. Ed. 62 (2023) e202306822.
[26] J.P. Dong, Y. Xu, X.G. Zhang, et al., Angew. Chem. Int. Ed. 62 (2023) e202313648.
[27] X.K. Wan, J.Q. Wang, Z.A. Nan, et al., Sci. Adv. 3 (2017) e1701823.
[28] X. Fan, K. Zuo, F. Yuan, et al., ACS Mater. Lett. 6 (2024) 1007–1011.
[29] Y. Jin, C. Zhang, X.Y. Dong, et al., Chem. Soc. Rev. 50 (2021) 2297–2319.
[30] Y.F. Zhang, Z.H. Zhang, L. Ritter, et al., J. Am. Chem. Soc. 143 (2021) 12202–12211.
[31] K. Wu, P.W. Cheng, X.Y. Liu, et al., Sci. China Chem. 67 (2024) 1000–1007.